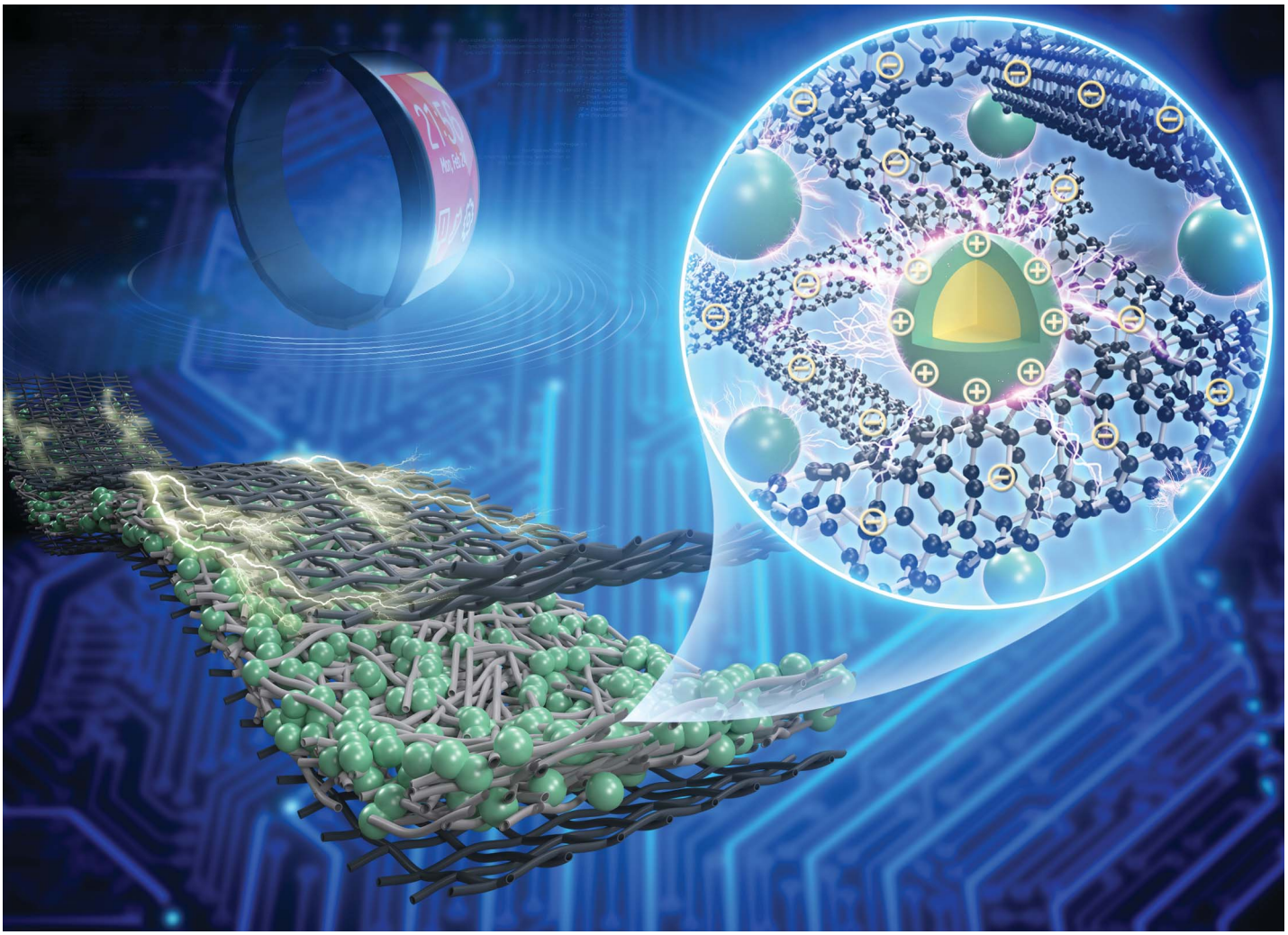

Highlighting a study on flexible silicon anodes by Zixin Hong, Dr. Zhenhan Fang, Prof. Jiaping Wang, and co-workers, Department of Physics and Tsinghua-Foxconn Nanotechnology Research Center, Tsinghua University.

Promising nano-silicon anodes prepared using the "disperse-anchor" strategy and functional carbon nanotube interlayers for flexible lithium-ion batteries

High performance Si anodes with stable cycling and favourable flexibility are achieved by surface modification and structural design. A "disperse-anchor" strategy is proposed to construct homogeneous Si anodes by electrostatic interaction. Lightweight CNT interlayers are covered on the Si anode to alleviate the active material loss and promote cycling stability. The $LiFePO_4$||Si pouch cell exhibits excellent flexibility after 10 000 times of bending.

As featured in:

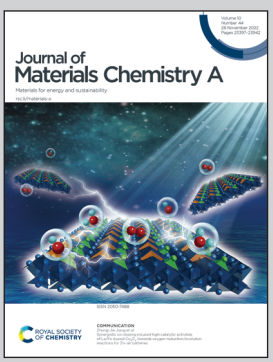

See Zhenhan Fang, Jiaping Wang *et al.*, *J. Mater. Chem. A*, 2022, **10**, 23509.

ROYAL SOCIETY OF CHEMISTRY

rsc.li/materials-a

Registered charity number: 207890

Journal of Materials Chemistry A

ROYAL SOCIETY OF CHEMISTRY

PAPER

Cite this: *J. Mater. Chem. A*, 2022, **10**, 23509

Promising nano-silicon anodes prepared using the "disperse-anchor" strategy and functional carbon nanotube interlayers for flexible lithium-ion batteries†

Zixin Hong,[a] Zhenhan Fang,*[a] Yufeng Luo,[b] Hengcai Wu,[a] Hui Tian,[a] Fei Zhao,[a] Qunqing Li,[ac] Shoushan Fan[a] and Jiaping Wang *[ac]

Nano-silicon (nano-Si) is considered a favorable candidate for next-generation lithium-ion batteries (LIBs) due to its high specific capacity, low discharge potential, and improved tolerance to volume changes. However, severe aggregation constitutes substantial impediments. In this work, first, a "disperse-anchor" strategy is proposed to improve the homogeneity of nano-Si electrodes. Positively charged polyaniline (PANI)-coated nano-Si (SiPA) and negatively charged super-aligned carbon nanotubes (SACNTs) construct the SiPA/CNT anode under the electrostatic interaction. Second, lightweight CNT interlayers are covered on the SiPA/CNT anode to alleviate the active material loss and promote cycling stability. Afterward, the SiPAC/CNT-film anode is obtained by transforming PANI into carbon through carbonization and exhibits an areal specific capacity of 2.77 mA h cm^{-2} at the 100th cycle. Moreover, the self-supporting CNT network contributes to excellent flexibility. After 10 000 cycles of 90° and 180° bending, the resistance of the SiPAC/CNT anode changes by only 2.66% and 3.14%, respectively. The pouch cell assembled with the $LiFePO_4$ cathode and SiPAC/CNT-film anode maintains more than 96% capacity after 10 000 times of 90° bending. The "disperse-anchor" strategy and CNT interlayer effectively enhance the cycling stability and flexibility of nano-Si anodes, which are promising in the development of flexible commercial LIBs.

Received 16th August 2022
Accepted 12th October 2022

DOI: 10.1039/d2ta06478b

rsc.li/materials-a

1. Introduction

With the development of advanced energy storage fields such as electric vehicles and large power grids in recent years, the demand for energy storage devices such as lithium-ion batteries (LIBs) with high energy density has become increasingly urgent.[1–4] Silicon (Si) has attracted much attention due to its extremely high theoretical specific capacity of 4200 mA h g^{-1} ($Li_{22}Si_5$),[5] abundant reserves,[6] and a lithiation potential of 0.2–0.3 V *vs.* Li/Li^+ (ref. 7) that avoids excessive lithium deposition.

However, Si also possesses many defects: (1) tremendous volume variation: The Si alloying/de-alloying process suffers from critical relative volume variation (300%),[8] which leads to cracking and crushing,[9] solid electrolyte interphase (SEI) instability,[10] continuous electrolyte consumption,[11,12] and eventually rapid capacity decay. For conventional electrodes, the slurry consists of the active material, conductive additive, and binder and is coated on the current collector. Severe volume changes in Si during cycling can easily cause the electrode to crack and detach from the current collector. (2) Poor electrical conductivity: Si exhibits a low electrical conductivity (~10^{-3} S cm^{-1}), which also hinders its commercial application.[13]

To address these problems, researchers have proposed various strategies, such as composite Si anodes,[14–16] nano-silicon (nano-Si) anodes,[17] and new binders.[18] Nano-Si has received widespread attention for simultaneously reducing volume variation and increasing conductivity: (1) nano-Si can better withstand the mechanical stress caused by volume change and effectively avoid particle pulverization.[19] (2) Nano-scale particles shorten the electronic transport path and enhance conductivity.[20,21] Typical nanostructures include Si nanospheres,[22] Si nanowires,[23] Si nanotubes,[24] and Si nano-films.[25] Nevertheless, nano-Si tends to aggregate, which is detrimental to electron transport at the phase interface.[26] The aggregation problem can usually be solved by surface treatment or by compositing with other materials. Seong-Hyeon Hong *et al.* treated Si with piranha solution to enrich its surface with –OH groups, thereby inhibiting aggregation.[27] Guo *et al.*

[a]*Department of Physics and Tsinghua-Foxconn Nanotechnology Research Center, Tsinghua University, Beijing, 100084, China. E-mail: fzh17@mails.tsinghua.edu.cn; jpwang@tsinghua.edu.cn*

[b]*Institute of Textiles and Clothing, Hong Kong Polytechnic University, Hong Kong, China*

[c]*Frontier Science Center for Quantum Information, Beijing, 100084, China*

† Electronic supplementary information (ESI) available. See DOI: https://doi.org/10.1039/d2ta06478b

composited Si, flake graphite, and pitch at high temperature and pressure to obtain robust Si/C microspheres.[28]

Additionally, the volume variation and poor conductivity of Si also pose a great challenge for electrode preparation. For conventional electrodes, novel binders and current collectors are promising research directions. New binders are dedicated to maintaining the integrity of the electrode structure and preventing the separation of particles from each other and the current collector, and the common types are carboxymethyl cellulose (CMC),[29] polyacrylic acid (PAA),[30] sodium alginate (SA),[31] and their mixture.[32,33] By making the surface rough[34] and porous,[35] the new current collector can increase the surface area, thus enhancing the bond with the slurry and maintaining good electrical contact during the cycle. Furthermore, some self-supporting electrodes without additional binder and current collector have been proposed.[36,37] They display promising flexibility capability, which is of great importance today when wearable and bendable electronic devices are vigorously promoted.

Si anodes with excellent performance are promising electrode materials for application in electronic products. With the rapid development of electronic devices in recent years, the flexibility of devices has been required. There have been some reported studies on flexible Si-based composites and bendable Si anodes lately, yet the preparation is often difficult and hazardous.[37–40] Therefore, it is essential to design feasible methods to fabricate flexible Si anodes and fully characterize the flexibility performance. The flexibility of electrodes can usually be achieved in terms of electrode materials and electrode structures. Firstly, flexible materials can be used as substrates, such as carbon materials,[41–43] MXene,[44] polymer materials,[45] textile materials,[46] *etc.* Secondly, special electrode structures can also be adopted, such as paper-cut structures,[47] wave structures,[48] fiber structures,[49] sponge structures,[50] island structures,[51] fabric structures,[52] and so on. Among them, super-aligned carbon nanotubes (SACNTs) have received wide attention, which have a high aspect ratio, clean surface, and strong van der Waals forces.[53,54] Macroscopic carbon materials such as flexible CNT-films, filter membranes, deposited membranes, and aerogels can be prepared based on SACNTs.[55,56] These macroscopic carbon materials exhibit excellent electrical and mechanical properties[57] and have been successfully applied in flexible composite electrodes,[42,58] current collectors,[41,59] and interlayers.[60,61]

In this work, we propose a "disperse-anchor" strategy and a functional interlayer to solve the issues of the nano-Si anode. First, the "disperse-anchor" strategy is used to mitigate the aggregation problem and improve the homogeneity of the Si/C flexible anodes by utilizing the electrostatic interaction. The positively charged nano-silicon coated with polyaniline (SiPA) is ultrasonically dispersed in the negatively charged CNTs, and both finite element simulations and experimental results verify that homogeneous anchoring of SiPA particles on CNTs can be achieved by electrostatic interaction. Afterward, polyaniline (PANI) transforms to carbon by high-temperature carbonization and wraps around the well-dispersed nano-Si, which improves the electrical conductivity of the anode. Finally, the combination of a convenient vacuum extraction process and an ultra-light SACNT functional interlayer results in a flexible and self-supporting film without any additional binder, conductive additive, and current collector. The preparation method of flexible electrodes is easy and universal. The size and shape of the flexible electrode are adjustable. Bending flexibility properties of both electrodes and pouch cells are characterized. The promising Si anode displays favorable electrochemical performance and excellent flexibility, demonstrating great potential as a candidate for next-generation flexible commercial LIBs.

2. Experimental

2.1. Preparation of SACNTs

SACNTs are prepared by chemical vapor deposition with iron as the catalyst and acetylene as the precursor.[62,63] The SACNT arrays are 30 nm in tube diameter and 300 μm in height. The clean walls and strong van der Waals forces of the SACNTs allow the extraction of continuous CNT-films from SACNT arrays by an "end-to-end" joining mechanism.[41]

2.2. Preparation of Si–NH_2, SiPA, and SiPAC

2.2.1. Si–NH_2. Solution A: 1.5 g nano-Si (20–80 nm, Aladdin) and 250 mL ethanol are mixed and ultrasonically dispersed for 20 min. Solution B: 15 mL ammonia (14.5 mol L^{-1}, FengChuan, Tianjin) is mixed with 75 mL deionized water. Solution B is slowly added to solution A and the mixture is stirred magnetically for 30 min. After that, 2.375 g (3-aminopropyl)triethoxysilane (APTES, Alfa Aesar) is added dropwise and stirred for 2 h. The composite is collected by centrifugation, followed by several washes with ethanol, and the precipitate is dried overnight at 50 °C. Nano-silicon powder with surface amination (Si–NH_2) is obtained after collecting and grinding. The molar ratio of APTES to Si is determined as 1 : 5 with reference to the experimental results of Huang *et al.*[64]

2.2.2. SiPA. Solution C: 1.4 g Si–NH_2 and 200 mL ethanol are mixed and sonicated for 15 min, after which 0.01 mol aniline (YongDa, Tianjin) is added, and sonication is continued for 30 min. Solution D: 5.6 g ammonium persulfate (JingChun, Beijing) is dissolved in 40 mL hydrochloric acid (1.4 mol L^{-1}, GaoHeng). Solution D is slowly added to solution C at 0 °C. Magnetic stirring is maintained at 0 °C for 4 h to achieve *in situ* coating of PANI on the surface of Si–NH_2. The mixture is washed by centrifugation several times, and the collected precipitate is dried overnight at 50 °C and ground to obtain SiPA. Different amounts of PANI are coated on Si–NH_2 to achieve $SiPA_{0.005}$ and $SiPA_{0.015}$ by using 0.005 mol aniline and 0.015 mol aniline, respectively. The mass percentages of Si in the $SiPA_{0.005}$, SiPA, and $SiPA_{0.015}$ are 51.1%, 45.5%, and 39.4%, respectively (Fig. S1†).

2.2.3. SiPAC. SiPA is heated in a tube furnace under an argon atmosphere and maintained at 900 °C for 3 h to obtain amorphous carbon-coated nano-silicon (SiPAC) after the pyrolysis of PANI. $SiPA_{0.005}$ and $SiPA_{0.015}$ are thermally treated with the same scheme to obtain $SiPAC_{0.005}$ and $SiPAC_{0.015}$.

2.3. Preparation of Si/CNT, Si/CNT-film, SiPA/CNT, SiPA/CNT-film, SiPAC/CNT, SiPAC/CNT-film, and Si-slurry electrodes

30 mg nano-Si, 10 mg SACNT, and 60 mL ethanol are mixed and sonicated for 30 min, and Si/CNT is obtained by vacuum filtration. 10-Layer cross-stacked SACNT films are covered on each side of the Si/CNT to obtain the Si/CNT-film and the mass loading of Si is about 3 mg cm^{-2}.

Based on the above steps, SiPA/CNT and the SiPA/CNT-film are also obtained with 30 mg SiPA and 10 mg SACNT. After carbonization (as presented in Section 2.2.3), SiPAC/CNT and the SiPAC/CNT-film are produced with the Si mass loading of 1.2–2 mg cm^{-2} and the Si content of 45.0% (Fig. S2†). Similarly, $SiPA_{0.005}$/CNT, $SiPA_{0.015}$/CNT, the $SiPAC_{0.005}$/CNT-film, and the $SiPAC_{0.015}$/CNT-film are acquired. All films are cut into 10 mm diameter discs to obtain the flexible electrodes without additional binder and current collector. The specific capacities are all calculated based on the mass of Si and the de-lithiation capacity.

Nano-Si, Super-P, and CMC (Macklin) are mixed in water at a mass ratio of 8 : 1 : 1, and then, a certain amount of aqueous CNT dispersion is added to obtain a homogeneous slurry with CNT contents of 0%, 12.5 wt%, and 25.0 wt%, respectively. The homogeneous slurry is coated on a copper current collector, dried at 60 °C for 2 h, and then transferred to a vacuum oven at 120 °C to remove water. The Si electrode sheet containing 0%, 12.5%, and 25.0% CNT is named Si-$slurry_{CNT=0}$, Si-$slurry_{CNT=12.5\%}$, and Si-$slurry_{CNT=25.0\%}$, respectively, and used for bending performance tests.

2.4. The assembly of coin cells

CR2025 coin cells are assembled in an argon glove box (M. Braun Inert Gas System Co. Ltd., Germany). The Si/CNT, SiPA/CNT, SiPAC/CNT, Si/CNT-film, SiPA/CNT-film, or SiPAC/CNT-film electrode serves as the anode, lithium foil is the cathode, and commercial PP film is the separator. The electrolyte is 1 M $LiPF_6$ in FEC : HFE : FEMC (2 : 2 : 6 by mass).

2.5. The assembly of pouch cells

Pouch cells are assembled in an argon glove box (M. Braun Inert Gas System Co. Ltd., Germany).

2.5.1. SiPAC//Li pouch cell. SiPAC/CNT-film (diameter: 38 mm), lithium sheet (side length: 40 mm), and commercial PP separator are packaged in the aluminum-plastic film, injected with electrolyte, and then vacuum heat pressed.

2.5.2. SiPAC//LFP pouch cell. 35 mg SACNT and 350 mg LFP are sonicated and vacuum filtered to produce the LFP/CNT-film. The SiPAC/CNT-film is first pre-lithiated.[65,66] It is wetted in the electrolyte, wrapped with an lithium sheet, and encapsulated in an aluminum-plastic pouch bag with an additional 200 μL of electrolyte. The pouch cell is pressed between two polytetrafluoroethylene (PTFE) plates and rested for 12 h to allow sufficient contact between the SiPAC/CNT-film and lithium sheet. Then, it is unpacked and the full cell is assembled: the pre-lithiated SiPAC/CNT-film, LFP/CNT-film, and commercial PP separator are placed in the aluminum-plastic film, followed by electrolyte injection and encapsulation.

2.6. Material analysis

Zeta potential is tested using powder dispersed in ethanol by using a nanoparticle size and zeta potential meter (Malvern, ZS90, China). Microscopic morphology is characterized by using a scanning electron microscope (SEM, Sirion 200, FEI) and a transmission electron microscope (TEM, Tecnai G2F20, FEI). The crystal structure is obtained by X-ray diffraction (XRD) using a diffractometer (Rigaku, Cu Kα radiation) in the 2θ range from 10° to 80°. Thermogravimetric analysis (TGA) is performed using a Pyris 1 TGA (PerkinElmer, USA) in air at a heating rate of 10 °C min^{-1} in the range of 25 °C to 900 °C. Raman spectroscopy is conducted using a Raman spectrometer (LabRam-HR/VV, JY) based on a 514 nm He–Ne laser. The square resistance of the powder and electrodes is obtained by a four-probe method. The resistance of the film is tested in real time using Ke 2400S software during the bending test (LANWAN Precision Instruments Co., Ltd) for 0–90° and 0–180°: the Si-slurry and SiPAC/CNT-films are cut into 2 cm × 6 cm strips and connected to the data collector using conductive silver glue to attach wires at both ends of the strips. The wetting behaviors of the SiPAC/CNT and SiPAC/CNT-film are characterized by measuring the contact angles of organic solvent droplets (5 μL). Tensile tests are conducted using an Instron 5848 microtester with a strain rate of 1% min^{-1} and a 1 cm gauge length.

2.7. Electrochemical measurements

Galvanostatic performances are tested by using a Land battery system (Wuhan Land Electronic Co., China) in the voltage range of 0.01–2.0 V (half cell) and 2.2–4.2 V (full cell). Electrochemical impedance spectroscopy (EIS) is performed using an electrochemical workstation (EG&G Princeton Applied Research 273A) at 2 mV ac amplitude in the frequency range of 100 mHz to 100 kHz. The galvanostatic intermittent titration technique (GITT) is conducted by using a Land battery system using a series of pulsed currents: 100 s of 1 A g^{-1} current, followed by 1800 s of relaxation. The diffusion coefficient (D_{Li^+}) is calculated based on the second lithiation and de-lithiation processes to avoid the influence of SEI.

2.8. Finite element simulation

Electrochemical models are constructed using an electrostatic module of COMSOL Multiphysics 5.6. Based on the finite element solver, the dispersion of particles with different charges is calculated. The SACNT is immobilized (*i.e.*, a relative coordinate system centered on the SACNT is set), and two active particles are placed at a certain position from it. The boundary potentials of the SACNT and active particles are given as zeta potentials. Based on the potential distribution, the spatial electric field is calculated, and the electric field force, acceleration, and displacement of the active material with time are calculated.

3. Results and discussion

With a high theoretical capacity, low discharge potential, and the ability to reduce volume variation, nano-Si stands out as a highly promising electrode material. For preparing electrodes, the common method is to mix the active material with the conductive agent and binder in a certain ratio and then apply it to the metal current collector. Unfortunately, it would introduce a large amount of inactive material, and the electrode could not tolerate folding. SACNTs are carbon nanotubes arranged very neatly in arrays, based on which many flexible electrodes are obtained without additional conductive agents, binders, and collectors.[67–69] In this case, SACNT and nano-Si are chosen to fabricate the Si anode.

3.1. "Disperse-anchor" strategy for agglomerated nano-Si

Nano-Si exhibits many advantages; nevertheless, it suffers from serious agglomeration.[26] The SEM image of commercial Si powder with a diameter of 20–80 nm in Fig. 1a shows that the

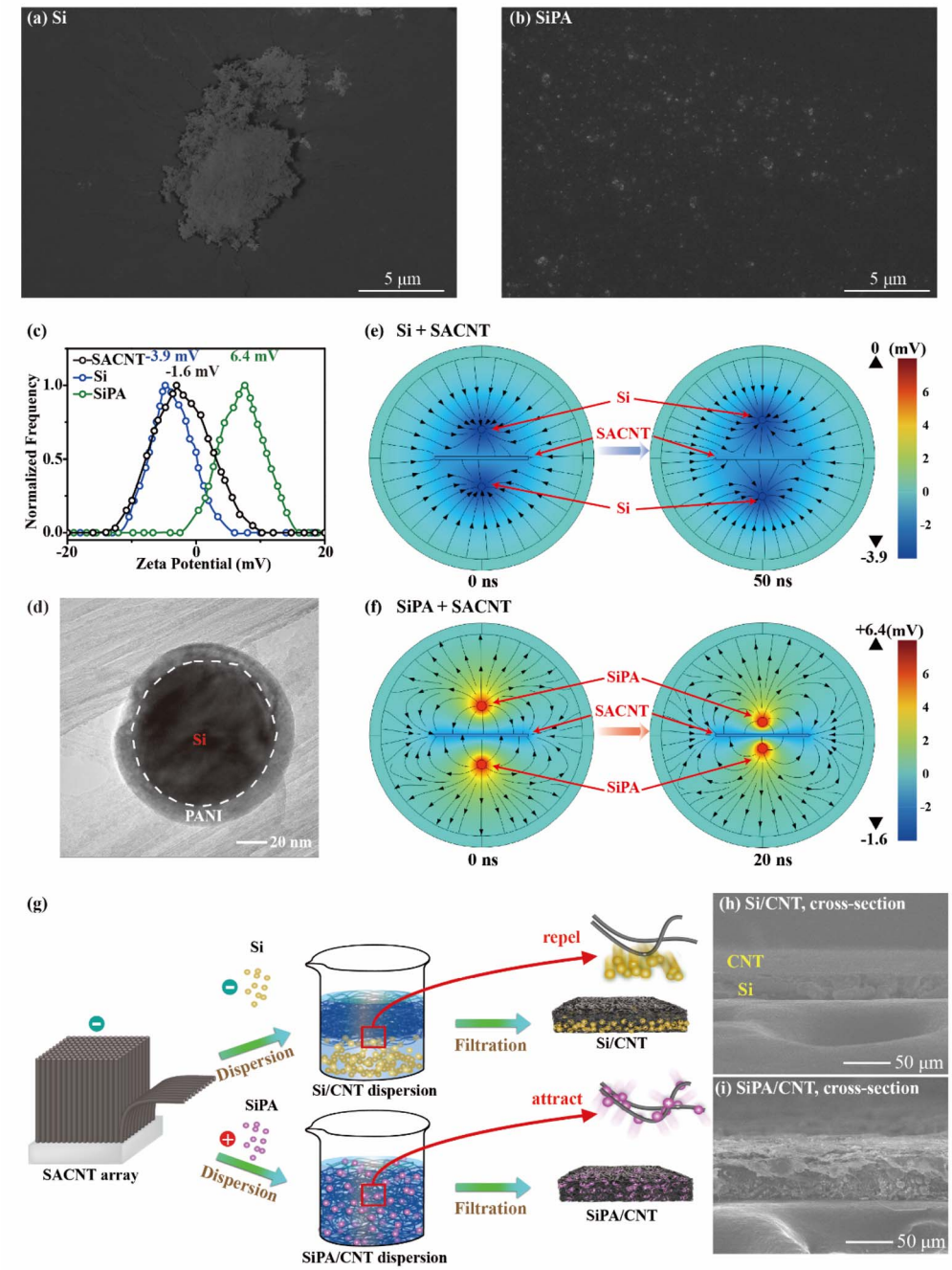

Fig. 1 (a) SEM of Si and (b) SiPA. (c) Zeta potentials of SACNT, Si, and SiPA. (d) TEM of SiPA. (e) Finite element simulation results of the dispersion of Si and SACNT at 0 ns and 50 ns. (f) Finite element simulation results of the dispersion of SiPA and SACNT at 0 ns and 20 ns. (g) Preparation process of Si/CNT and SiPA/CNT. (h) Cross-section SEM images of a Si/CNT anode and (i) a SiPAC/CNT anode.

nano-Si agglomerates into clusters of several microns in size. The dispersion stability of nanoparticles is determined by a combination of attractive van der Waals interaction and repulsive electrostatic interaction according to the Derjaguin–Landau–Verwey–Overbeek (DLVO) theory.[70] Electrostatic interaction mainly derives from the electrical double layer. Particles with the same charge in solution form an electrical double layer on the surface, and when two particles approach one another, electrostatic repulsive interaction occurs.[71] The surface charging of the particles can be characterized by the zeta potential.[72] The smaller the absolute value of the zeta potential, the weaker the electrostatic repulsion. The zeta potential of nano-Si is −3.9 mV (Fig. 1c), and its aggregation may be due to insufficient electrostatic repulsion.

To avoid the agglomeration of nano-Si and to prepare homogeneous electrodes, a "disperse-anchor" strategy is proposed. Primarily, to promote the dispersion of nano-Si, surface modification can be performed to increase the absolute value of zeta potential and enhance the electrostatic repulsion between particles. Meanwhile, for the preparation of uniform electrodes, it is necessary to consider the charges of each component. Both SACNTs and nano-Si are negatively charged, and the zeta potentials are −1.6 mV and −3.9 mV, respectively (Fig. 1c), discouraging the close bonding of SACNTs and nano-Si. If the surface of nano-Si is modified to carry a positive charge, then it is oppositely charged with SACNTs. Thereby, SACNTs and the modified nano-Si powder can be "dispersed" by their respective electrostatic repulsion and "anchored" by their mutual electrostatic attraction, which is the "disperse-anchor" strategy.

When applying this strategy, the first step is to select a material that is positively charged and carries a larger charge (specifically: a bigger absolute value of zeta potential). PANI is a suitable candidate for its ability to be wrapped on the surface of the host material easily and uniformly by the *in situ* polymerization.[73] As nano-Si powders are easily aggregated, they can be treated with APTES to acquire Si–NH_2 and to improve the coating performance of PANI.[64,74,75] TEM images of Si and Si–NH_2 are shown in Fig. S3,† revealing the successful surface modification. Then, the SiPA is obtained by coating PANI on the Si–NH_2. Fig. 1d displays a TEM image of SiPA with a PANI layer of about 10 nm. By varying the amount of aniline, $SiPA_{0.005}$, SiPA, and $SiPA_{0.015}$ with different thicknesses of PANI coating can be obtained (Fig. S4a–c†). The energy-dispersive spectroscopy (EDS) element mapping images for C, N, O, and Si are shown in Fig. S3g–i,† demonstrating that PANI coating of $SiPA_{0.005}$, SiPA, and $SiPA_{0.015}$ is gradually thickened. After that, the zeta potential of the sample is tested. With the PANI coating, the zeta potential of SiPA is +6.4 mV, compared to that of −3.9 mV for Si (Fig. 1c). The absolute value of zeta potential gets larger, indicating a greater electrostatic repulsion between SiPA particles for better dispersion. As the SEM image in Fig. 1b reveals, SiPA particles are uniformly dispersed. In addition, SACNTs and SiPA are oppositely charged and are expected to be tightly bonded.

The effectiveness of the "disperse-anchor" strategy is verified by both simulation and experiment. First, finite element simulations are performed. Fig. S5† shows the model diagram of finite element simulation (see Table S1† for detailed parameters). The rectangle represents SACNT, the two small circles stand for Si or SiPA, and the zeta potentials of Si/SiPA and SACNT form an electrostatic field. There exists an initial distance of d between the Si/SiPA and SACNT, and the motion of Si/SiPA is generated by the electrostatic force, which in turn changes the electrostatic field and electrostatic force. With colors representing the potential and flow lines symbolizing the electric field lines, the finite element simulation results are demonstrated in Fig. 1e and f (see Videos S1 and S2† for the complete simulation process). Fig. 1e simulates the dispersion of Si and SACNTs: the potential ranges from −3.9 mV (Si) to 0 mV (boundary), and the Si moves away from the SACNTs under the electrostatic repulsion at 50 ns. Fig. 1f emulates the dispersion of SiPA and SACNTs: the potential range is −1.6 mV (SACNTs) to 6.4 mV (SiPA), and SiPA approaches SACNTs under electrostatic attraction at 20 ns. These simulation results demonstrate that Si and SACNTs with the same charge repel one another, and SiPA and SACNTs with different charges attract one another, demonstrating the validity of the "disperse-anchor" strategy.

Furthermore, the effectiveness of the "disperse-anchor" strategy is examined by experiments. Fig. 1g illustrates the preparation processes of Si/CNTs and SiPA/CNTs: SACNTs, active material (Si/SiPA), and ethanol are ultrasonically dispersed, and flexible self-supporting Si/CNT and SiPA/CNT-films are acquired by rapid vacuum filtration. This method is convenient and efficient, and different sizes and shapes of films can be easily achieved by varying the dimensions of the filtration molds (Fig. S6†). CNT and Si carry the same charge, and the minor charge is not adequate to provide sufficient electrostatic repulsion for uniform dispersion. During vacuum filtration, the Si particles deposit onto the filter membrane initially, resulting in delamination of CNT and Si in the Si/CNT-film (Fig. 1h). In contrast, SACNTs and SiPA are heterogeneously charged, so they attract mutually and construct a homogeneous film (Fig. 1i).

3.2. SACNT functional interlayer

The problem of nano-Si aggregation is solved using a "disperse-anchor" strategy, where the active material inside the anode could be confined within the CNT network by the electrostatic interaction. Nevertheless, the active material adjacent to the surface may detach from the anode during the cycling process (Fig. 2a), leading to poor electrochemical performance.

The SACNT functional interlayer is proposed to reduce the shedding of the active material from the electrode. As shown in Fig. 2b, a CNT-film can be extracted from the SACNT array, and the density of a monolayer film is 1.5 μg cm^{-2}.[54,60] By layering each film in a perpendicular direction to each other, a cross-stacked film is obtained. The CNTs of the functional interlayer are oriented and densely aligned (Fig. 2d and e), which can effectively block the shedding of the active material from the anode. As illustrated in Fig. 2c, the SACNT functional interlayer is applied on both sides of the anode as a barrier. Since the SACNT interlayer possesses smaller pores than the SiPA particle

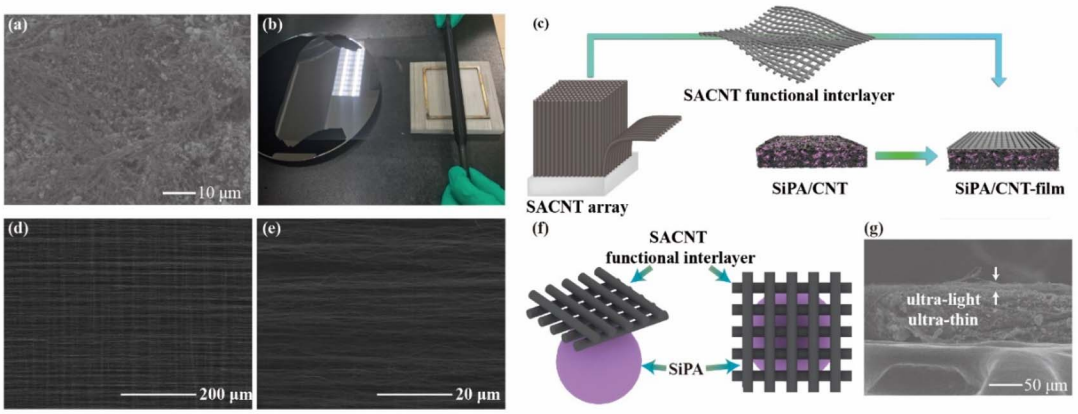

Fig. 2 (a) Surface SEM of the SiPA/CNT anode. (b) Optical photograph of a CNT-film drawn from the SACNT array. (c) Illustration of the electrode preparation using a SACNT functional interlayer. (d and e) SEM of a SACNT functional interlayer (10-layer cross-stacked) at different magnifications. (f) Diagram of the SACNT functional interlayer and SiPA. (g) Cross-section SEM of an anode with the SACNT functional interlayer.

size (~100 nm), reductions in active material losses are expected (Fig. 2f).

Experiments are performed to investigate whether the CNT functional interlayer can effectively preserve the active material from falling off. Without the interlayer, the Si particles of the Si/CNT anode fall off when the anode is shaken and tapped (Fig. S7a, Video S3†). However, this situation is no longer present when the CNT interlayer is applied (Fig. S7b, Video S4†). In addition, the interlayer is ultra-light and ultra-thin (Fig. 2g) and exhibits favorable wettability to organic solvents (Fig. S8†). These results demonstrate that the functional CNT interlayer can effectively serve as a surface protection barrier and is expected to improve the cycling stability of Si anodes without reducing energy density.

3.3. Carbonization

To further improve the conductivity, SiPAC is obtained by heating SiPA under an inert atmosphere, converting PANI to carbon. The square resistances of SiPA and SiPAC are 2.24×10^5 Ω sq^{-1} and 1.40×10^3 Ω sq^{-1}, respectively (Fig. 3a). The chemical structures of the powders are characterized by Raman spectroscopy (Fig. 3b). The peaks at 520 cm^{-1} and 945 cm^{-1} are characteristic peaks of Si. The 1170 cm^{-1} peak of SiPA and commercial PANI (Macklin) corresponds to C–H bending deformation in the quinoid/phenyl groups,[76] and 1340 cm^{-1} and 1585 cm^{-1} signals correspond to C–C and CC stretching in the quinoid rings, respectively.[77] In the Raman spectrum of SiPAC, all the characteristic peaks of PANI disappear, and the characteristic carbon D-peak (1352 cm^{-1}) and G-peak (1597 cm^{-1}) are detected.[73,78] In addition, a broad peak of 2700–3200 cm^{-1} exists in SiPAC, which is the second-order harmonic D′-band.[76] It signifies that PANI is completely transformed into carbon after carbonization, which can promote electrolyte penetration into the electrode and create more rapid diffusion paths for lithium ions.[73] Fig. S9† presents the XRD patterns of Si, SiPA, and SiPAC powders. The lattice structure of Si remains during the surface treatments and carbonization. Moreover, the XRD curves of both SiPA and SiPAC contain no peaks of silicon oxides. By combining the XRD and EDS results (Fig. S4†), it can be confirmed that the Si is covered with PANI and there is almost no silicon oxide.

The SiPAC/CNT-film is derived from the SiPA/CNT-film after carbonization, maintaining favorable dispersion of the active material with CNT (Fig. S10†). The CNT interlayer exhibits an intact structure and clean surface (Fig. 3g and i) and remains structural stability after 100 cycles (Fig. 3h and j). Carbonization enhances the performance of the anode in many ways. Firstly, the square resistance of the anode is reduced. The square resistances of the Si/CNT, SiPA/CNT, and SiPAC/CNT anodes are 12.4 Ω sq^{-1}, 4.3 Ω sq^{-1}, and 3.4 Ω sq^{-1}, respectively. Secondly, the diffusion coefficient D_{Li^+} of the anode is improved. The D_{Li^+} values of the Si/CNT-film, SiPA/CNT-film, and SiPAC/CNT-film anodes during the second lithiation and de-lithiation processes are calculated using the galvanostatic intermittent titration technique (GITT) (Fig. 3c and S11†) and vary in the ranges of 10^{-12} to 10^{-13} cm^2 s^{-1}, 10^{-10} to 10^{-13} cm^2 s^{-1}, and 10^{-9} to 10^{-13} cm^2 s^{-1}, respectively. A detailed description of the calculation method is illustrated in Fig. S12.† The SiPAC/CNT-film anode possesses a greater D_{Li^+}, indicating a better diffusion of lithium ions and possibly a better rate performance. During lithiation and de-lithiation process, the SiPA/CNT-film and SiPAC/CNT-film show minimal values of D_{Li^+} at about SOC = 25% and SOC = 75%. This phenomenon has been mentioned in other works, which is probably caused by two amorphous compositions (a-Li_7Si_3 and a-$Li_{13}Si_4$).[79–82] Finally, the contact resistance R_1 and the charge transfer resistance R_{ct} are lowered. Fig. 3d exhibits the EIS curves before cycling and the equivalent circuit. According to the fitted values of R_1 and R_{ct}, covering PANI and carbonization can effectively reduce the contact resistance R_1 and the charge transfer resistance R_{ct}. The EIS curves of the $SiPAC_{0.005}$/CNT-film and $SiPAC_{0.015}$/CNT-film anodes are shown in Fig. S13,† and they both have lower resistance than that of the Si/CNT-film anode. During cycling, the SiPAC/CNT-film anode displays the smallest R_1 and R_{ct} (Fig. 3e and f), implying the fastest reaction kinetics and promising better electrochemical performance.

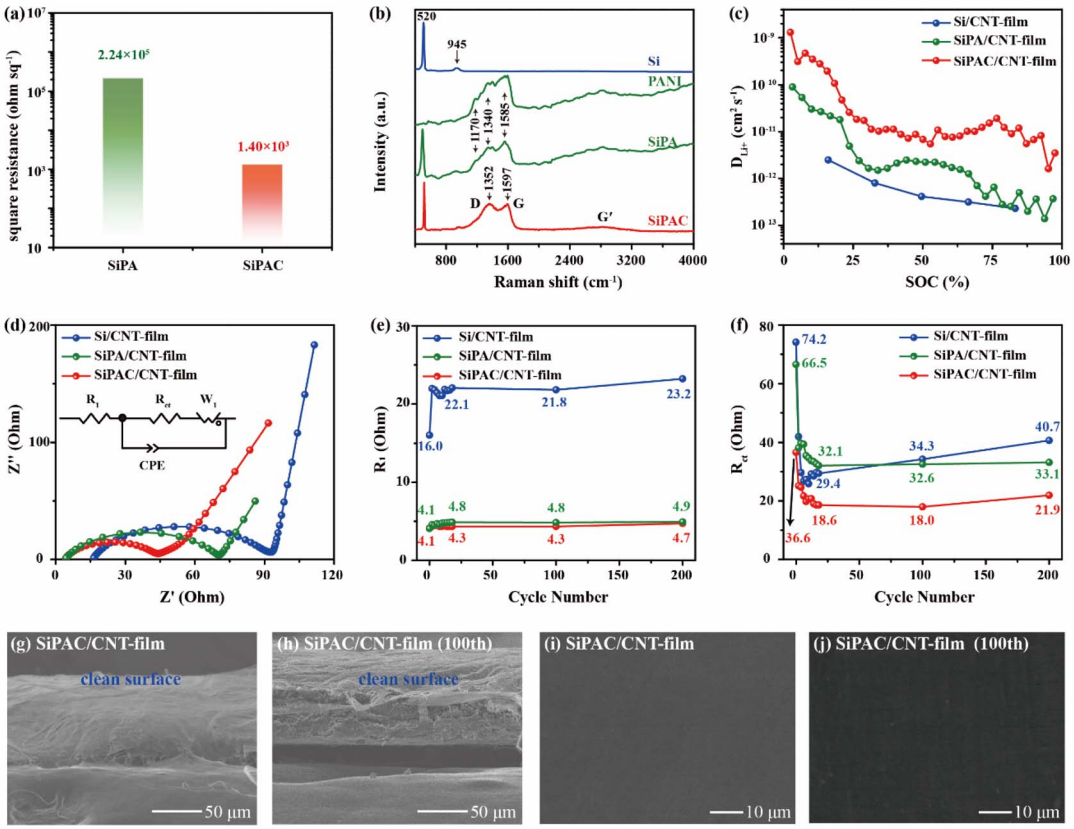

Fig. 3 (a) The square resistances of SiPA and SiPAC, (b) Raman spectra, (c) D_{Li^+} (based on the second lithiation process), and (d) EIS measurements of the Si/CNT-film, SiPA/CNT-film, and SiPAC/CNT-film anodes, (e) R_1 and (f) R_{ct} of the Si/CNT-film, SiPA/CNT-film, and SiPAC/CNT-film anodes during 0–200 cycles. (g) Cross-section SEM of a SiPAC/CNT-film anode before and (h) after 100 cycles. (i) Surface SEM of a SiPAC/CNT-film anode before and (j) after 100 cycles.

3.4. Electrochemical performance

Coin cells assembled with the flexible Si/CNT, Si/CNT-film, SiPAC/CNT, and SiPAC/CNT-film anodes are first activated at a current density of 0.2 A g^{-1} for 5 cycles and then cycled at a current density of 0.4 A g^{-1}. All specific capacities are calculated based on the mass of Si and the de-lithiation process. The cycling performance is presented in Fig. 4a. The Si/CNT anode exhibits an initial specific capacity of 1134.4 mA h g^{-1} and remains only 240.3 mA h g^{-1} after 50 cycles. The Si/CNT-film displays a slightly higher specific capacity than the Si/CNT anode, as the cross-stacked SACNT films on both sides mitigate the loss of active material. The specific capacity is only 325.2 mA h g^{-1} after 50 cycles. The coulombic efficiencies of Si/CNT and Si/CNT-film are unstable during cycling, probably because the cracked nano-Si exposes new interfaces in contact with the electrolyte and overconsumes the electrolyte.[11] Cells assembled with the SiPAC/CNT and SiPAC/CNT-film anodes display initial specific capacities of 1485.4 mA h g^{-1} and 1302.5 mA h g^{-1} and maintain 1046.6 mA h g^{-1} and 1164.5 mA h g^{-1} after 200 cycles, correspondingly. Moreover, the coulombic efficiencies are stable during the cycling process after the coating treatment of nano-Si. The initial coulombic efficiencies (ICEs) of the Si/CNT-film and SiPAC/CNT-film anodes are 48.7% and 54.7%, respectively, as shown in the charge–discharge curves (Fig. 4b). Improved ICE of SiPAC/CNT-film is facilitated by the faster electron and ion transport properties of SiPAC. After 200 cycles, the capacity retention percentages for the Si/CNT-film and SiPAC/CNT-film anodes are 13.9% and 89.4%, respectively. These results suggest the effective inhibition of the capacity decay of Si anodes by surface modification.

The cycling performances of the anodes with different PANI coating amounts are demonstrated in Fig. S14,† in which the SiPAC/CNT-film anode performs the best. The areal loading of Si increases from 1.19 mg cm^{-2} to 1.38, 1.72, and 1.99 mg cm^{-2} in the SiPAC/CNT-film anode. The areal specific capacities of the cells after 100 cycles are presented in Fig. 4c (see Fig. S15† for the detailed cycle capacity curves), which are advantageous compared with other silicon-carbon (Si–C) anodes in the literature (Table S2†).[83–93]

With positive PANI coating improving the homogeneity of the anode and the SACNT functional interlayer reducing the active material loss, the cycling stability of the SiPAC/CNT-film anode is effectively promoted. Meanwhile, the high-temperature carbonization increases D_{Li^+} and reduces R_1 and R_{ct}, and CNT provides a sufficient electron-conducting network and ion diffusion channels, which is expected to achieve faster reaction kinetics and exhibit better rate performance. As shown

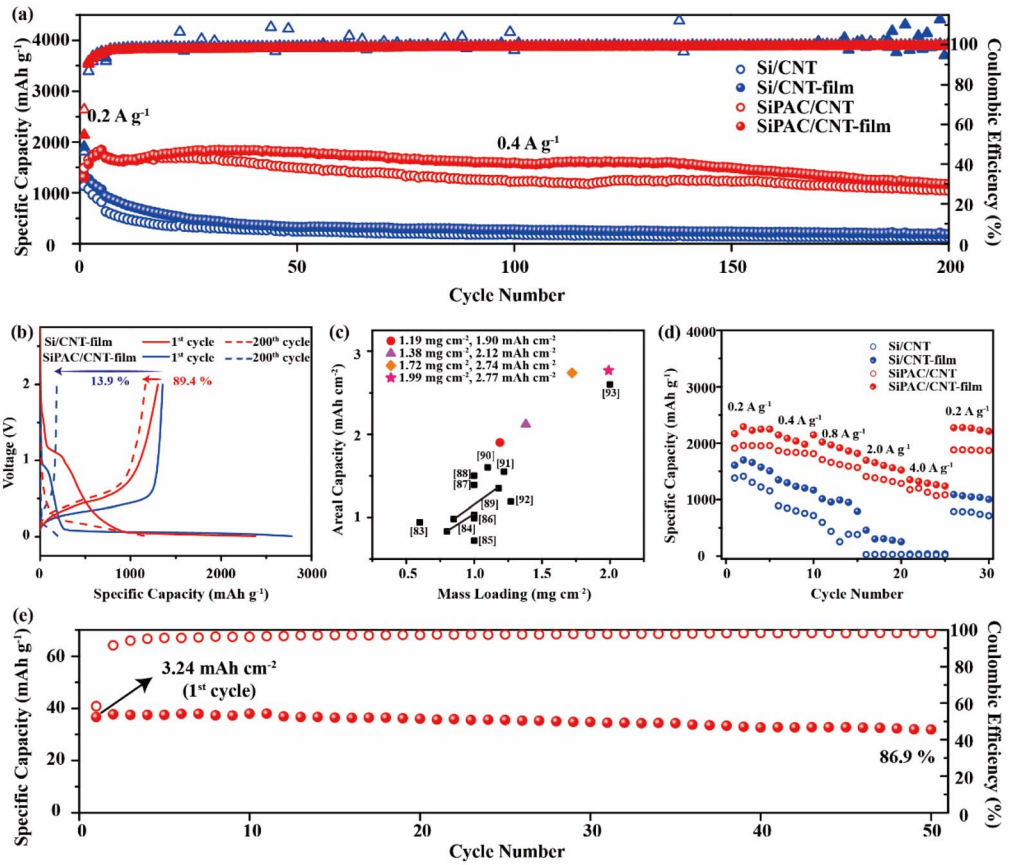

Fig. 4 (a) Cycling performance of the Si/CNT, Si/CNT-film, SiPAC/CNT, and SiPAC/CNT-film anodes. (b) Charge–discharge curves of the Si/CNT-film and SiPAC/CNT-film anodes at the 1st and 200th cycles. (c) Areal specific capacities of the SiPAC/CNT-film anodes with different areal loadings after 100 cycles and comparison with data in the literature. (d) Rate performances of the Si/CNT, Si/CNT-film, SiPAC/CNT, and SiPAC/CNT-film anodes. (e) Cycling performance of a SiPAC//Li pouch cell (0.4 A g^{-1}).

in Fig. 4d, the SiPAC/CNT-film anode exhibits specific capacities of 2247.3, 2146.8, 1817.7, 1520.0, and 1237.3 mA h g^{-1} at current densities of 0.2, 0.4, 0.8, 2.0, and 4.0 A g^{-1}, respectively. When the current density is returned to 0.2 A g^{-1}, the specific discharge capacity reverts to 2273.8 mA h g^{-1}, which is attributed to the excellent interlayer of the SiPAC/CNT-film anode that can effectively alleviate the active material loss. The capacity of the SiPAC/CNT anode is lower than that of the SiPAC/CNT-film, with a specific capacity of 1955.3 mA h g^{-1} at a current density of 0.2 A g^{-1}. When returning from 4.0 A g^{-1} to 0.2 A g^{-1}, the specific capacity of the SiPAC/CNT anode recovers to 1878.0 mA h g^{-1} with a capacity retention rate of 96.05%, which is less than that of the SiPAC/CNT-film anode, indicating the effectiveness of the cross-stacked SACNT films. The Si/CNT and Si/CNT-film anodes show poor rate performance with specific capacities of 18.5 mA h g^{-1} and 35.1 mA h g^{-1} at a current density of 4.0 A g^{-1}, respectively. When the current density is restored to 0.2 A g^{-1}, the capacity retention is 68.40% (787.6/1151.4 mA h g^{-1}) for the Si/CNT and 72.10% (1086.4/1506.8 mA h g^{-1}) for Si/CNT-film anodes. It is demonstrated that rapid lithiation/de-lithiation dramatically affects the electrochemical properties of nano-Si. The SiPAC/CNT-film anode exhibits the best rate performance, confirming that the strategies of PANI coating, carbonization, and interlayer enable fast reaction kinetics.

Along with coin cells, pouch cells also offer favorable cycle performance, revealing promising large-scale fabrication capability. The SiPAC//Li pouch cell exhibits a capacity of 36.69 mA h (3.24 mA h cm^{-2}) at a current density of 0.4 A g^{-1} in the first cycle and capacity retention of 86.9% after 50 cycles, which demonstrates commercial potential (Fig. 4e).

3.5. Flexibility performance

CNTs can be used to construct self-supporting anodes with no additional binder and current collector, which results in excellent flexibility. Fig. S16† shows optical photographs of the SiPAC/CNT-film in the flat, 180° bent, rolled, and recovered states, revealing its flexibility. The stress–strain curve of the SiPAC/CNT-film is shown in Fig. S17.† In this section, the resistances of the Si-slurry$_{CNT=0}$, Si-slurry$_{CNT=12.5\%}$, Si-slurry$_{CNT=25.0\%}$, and SiPAC/CNT strips in the long-cycle bending test are compared, and the flexibility performance of SiPAC//LFP pouch cells is characterized.

Long cycle bending of the Si-slurry$_{CNT=0}$, Si-slurry$_{CNT=12.5\%}$, Si-slurry$_{CNT=25.0\%}$, and SiPAC/CNT strips at 90° and 180° is

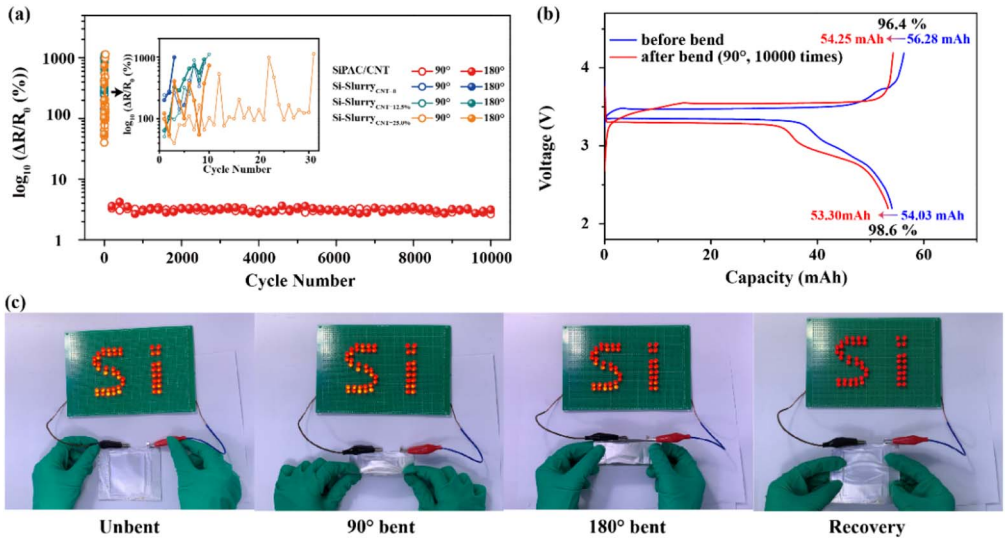

Fig. 5 (a) Normalized resistance changes of the SiPAC/CNT, Si-slurry$_{CNT=0}$, Si-slurry$_{CNT=12.5\%}$, and Si-slurry$_{CNT=25.0\%}$ strips during 10 000 cycles at 90° and 180° bending. (b) Voltage profiles of the SiPAC//LFP pouch cell before and after bending (0.2 A g^{-1}). (c) Photographs of the lit LED array using the flexible SiPAC//LFP pouch cell under different bending conditions.

performed using a bending life test machine, and the normalized resistance changes measured in real time are illustrated in Fig. 5a. The resistance of the SiPAC/CNT strip fluctuates within a small range during the long cycle, with incremental resistance of 2.66% (90°) and 3.14% (180°) after 10 000 bending cycles. As shown in the SEM image of the film before and after bending, the SiPAC/CNT strip has creases on the surface after 10 000 bends (Fig. S18b, c and Fig. S19b, c†), but the structure is still integral. The CNTs construct a flexible and robust mechanical skeleton, which enables the film to withstand long-cycle bending at large angles.

In contrast, the Si-slurry$_{CNT=0}$, Si-slurry$_{CNT=12.5\%}$, and Si-slurry$_{CNT=25.0\%}$ strips are not resistant to bending. For the Si-slurry$_{CNT=0}$ strip, the resistance increases by 779% for 9 bends at 90° and by 994% for 3 bends at 180°, followed by a dramatic rise. The surface of the Si-slurry$_{CNT=0}$ strip cracks after several bends at 90° and 180° (Fig. S18e and f†), and some of the active material detach from the current collector (Fig. S19e and f†), which causes fracture and a sharp increment in resistance. With the addition of CNT to the slurry, the Si-slurry$_{CNT=12.5\%}$ and Si-slurry$_{CNT=25.0\%}$ strips exhibit a smaller resistance change and better tolerance to bending. However, the resistance of the Si-slurry$_{CNT=12.5\%}$ strip increases sharply after 10 bends at 90° and 9 bends at 180°, and the Si-slurry$_{CNT=25.0\%}$ strip shows a substantial increase in resistance after 31 bends at 90° and 10 bends at 180°. After bending several times, both of them suffer from cracks (Fig. S18h, i, k and l†) and detachment from the copper current collector (Fig. S19h, i, k and l†). These results illustrate the excellent flexibility and durability of the novel SiPAC/CNT electrode compared to conventional electrodes utilizing slurry and metal collectors.

The SiPAC//LFP pouch cell is assembled with a pre-lithiated SiPAC/CNT-film anode and LFP/CNT-film cathode to perform the bending capacity retention test. As shown in Fig. 5b, the SiPAC//LFP pouch cell exhibits a charge capacity of 56.28 mA h and a discharge capacity of 54.03 mA h during the first charge–discharge. The discharge voltage curve decreases slightly at the later stage, which may be related to the relatively slow diffusion of lithium ions.[94] The energy density of the SiPAC//LFP pouch cell is 451 W h kg^{-1} (counting the mass of the electrodes). Due to the pre-lithiation, the ICE is 96.0%. Afterward, the pouch cell is bent at 90° 10 000 times (Video S5† shows part of the bending process). The pouch cell remains intact in appearance after bending (Fig. S20†) and presents a charge capacity of 54.25 mA h and a discharge capacity of 53.30 mA h. The 96.4% charge capacity retention and 98.6% discharge capacity retention of the SiPAC//LFP pouch cell strongly demonstrate the excellent flexibility of the SiPAC/CNT-film anode. Additionally, it could light up a LED array under different bending conditions (Fig. 5c, Video S6†).

4. Conclusions

In summary, the construction strategy of flexible Si anodes is proposed in terms of both surface modification and structural design. Si suffers from severe volume changes during cycling, which can lead to anode cracking and rapid capacity decay. Although nano-Si can better withstand the stresses caused by volume changes, it poses serious aggregation problems. Si also displays poor electrical conductivity and slow electrode kinetics. Coating PANI-derived carbon on the Si surface can solve these problems and improve the uniformity of the anode by the "disperse-anchor" effect between the positively charged SiPA and negatively charged SACNTs. With the functional CNTs, the SiPAC/CNT-film anode does not require any additional binder and current collector. The CNT skeleton provides a sufficient electron transport network, ion diffusion channels, reserved space for Si volume expansion, and robust three-dimensional

mechanical support. The CNT functional interlayer on both sides has been observed to effectively reduce active material shedding from the electrode surface. Owing to the surface modification and structural design, the SiPAC/CNT-film anode exhibits a specific capacity of 1164.5 mA h g^{-1} after 200 cycles, showing improved cycling stability. The anode with an areal loading of 1.99 mg cm^{-2} for nano-Si achieves a specific capacity of 2.77 mA h cm^{-2} after 100 cycles, demonstrating promising commercial potential. In addition, the Si anode based on this strategy exhibits excellent flexibility, with a resistance change of only 2.66% and 3.14% after 10 000 bends at 90° and 180°, respectively. The SiPAC//LFP pouch cell retains more than 96% capacity after 10 000 bends at 90°. The "disperse-anchor" and functional interlayer strategies present an effective solution to improve the homogeneity of the electrodes and contribute to the research of next-generation flexible Li-ion energy storage devices.

Author contributions

Zixin Hong: conceptualization, investigation, visualization, and writing – original draft. Zhenhan Fang: conceptualization, investigation, supervision, and writing – review & editing. Yufeng Luo: investigation. Hengcai Wu: investigation. Hui Tian: investigation. Fei Zhao: investigation. Qunqing Li: supervision. Shoushan Fan: supervision. Jiaping Wang: conceptualization, supervision, writing – review & editing.

Conflicts of interest

There are no conflicts to declare.

Acknowledgements

This work was supported by the National Basic Research Program of China (2019YFA0705702) and the National Natural Science Foundation of China (51872158).

References

1 T. Kim, W. Song, D.-Y. Son, L. K. Ono and Y. Qi, *J. Mater. Chem. A*, 2019, **7**, 2942–2964.
2 F. Wu, J. Maier and Y. Yu, *Chem. Soc. Rev.*, 2020, **49**, 1569–1614.
3 H. Liu, J. Wang, W. Hua, L. Ren, H. Sun, Z. Hou, H. Yu, Y. Cao, C. Wei and F. Kang, *Energy Environ. Sci.*, 2022, **15**, 1872–1881.
4 M. Jiang, Z. Hou, J. Wang, L. Ren, Y. Zhang and J. Wang, *Nano Energy*, 2022, **102**, 107708.
5 Y. Chen, S. Zeng, J. Qian, Y. Wang, Y. Cao, H. Yang and X. Ai, *ACS Appl. Mater. Interfaces*, 2014, **6**, 3508–3512.
6 F. Ebner and L. Greb, *Chem*, 2021, **7**, 2151–2159.
7 M. Gu, Y. He, J. Zheng and C. Wang, *Nano Energy*, 2015, **17**, 366–383.
8 A. Y. R. Prado, M.-T. F. Rodrigues, S. E. Trask, L. Shaw and D. P. Abraham, *J. Electrochem. Soc.*, 2020, **167**, 160551.
9 D. Liu, Z. Liu, X. Li, W. Xie, Q. Wang, Q. Liu, Y. Fu and D. He, *Small*, 2017, **13**, 1702000.
10 K. Zhang, Y. Tian, C. Wei, Y. An and J. Feng, *Appl. Surf. Sci.*, 2021, **553**, 149566.
11 E. Peled and S. Menkin, *J. Electrochem. Soc.*, 2017, **164**, A1703.
12 W. Tao, P. Wang, Y. You, K. Park, C.-Y. Wang, Y.-K. Li, F.-F. Cao and S. Xin, *Nano Res.*, 2019, **12**, 1739–1749.
13 Z. Liu, S. Bai, B. Liu, P. Guo, M. Lv, D. Liu and D. He, *J. Mater. Chem. A*, 2017, **5**, 13168–13175.
14 X. Shen, Z. Tian, R. Fan, L. Shao, D. Zhang, G. Cao, L. Kou and Y. Bai, *J. Energy Chem.*, 2018, **27**, 1067–1090.
15 Z. Zhao, J. Han, F. Chen, J. Xiao, Y. Zhao, Y. Zhang, D. Kong, Z. Weng, S. Wu and Q. Yang, *Adv. Energy Mater.*, 2022, 2103565.
16 J. Guo, W. Zhai, Q. Sun, Q. Ai, J. Li, J. Cheng, L. Dai and L. Ci, *Electrochim. Acta*, 2020, **342**, 136068.
17 X. H. Liu, L. Zhong, S. Huang, S. X. Mao, T. Zhu and J. Y. Huang, *ACS Nano*, 2012, **6**, 1522–1531.
18 S. Li, Y.-M. Liu, Y.-C. Zhang, Y. Song, G.-K. Wang, Y.-X. Liu, Z.-G. Wu, B.-H. Zhong, Y.-J. Zhong and X.-D. Guo, *J. Power Sources*, 2021, **485**, 229331.
19 B. Liang, Y. Liu and Y. Xu, *J. Power Sources*, 2014, **267**, 469–490.
20 F. H. Du, K. X. Wang and J. S. Chen, *J. Mater. Chem. A*, 2016, **4**, 32–50.
21 L. Sun, J. Xie and Z. Jin, *Energy Technol.*, 2019, **7**, 1900962.
22 S. Wang, X. Xiao, Y. Zhou, C. Fu and S. Jiao, *Electrochim. Acta*, 2018, **282**, 946–954.
23 S. Karuppiah, C. Keller, P. Kumar, P.-H. Jouneau, D. Aldakov, J.-B. Ducros, G. Lapertot, P. Chenevier and C. Haon, *ACS Nano*, 2020, **14**, 12006–12015.
24 M. H. Park, M. G. Kim, J. Joo, K. Kim, J. Kim, S. Ahn, Y. Cui and J. Cho, *Nano Lett.*, 2009, **9**, 3844–3847.
25 F. Le Cras, B. Pecquenard, V. Dubois, V.-P. Phan and D. Guy-Bouyssou, *Adv. Energy Mater.*, 2015, **5**, 1501061.
26 P. Li, H. Kim, S. T. Myung and Y. K. Sun, *Energy Storage Mater.*, 2021, **35**, 550–576.
27 C.-H. Jung, K.-H. Kim and S.-H. Hong, *ACS Appl. Mater. Interfaces*, 2019, **11**, 26753–26763.
28 J.-Y. Li, G. Li, J. Zhang, Y.-X. Yin, F.-S. Yue, Q. Xu and Y.-G. Guo, *ACS Appl. Mater. Interfaces*, 2019, **11**, 4057–4064.
29 Z. Yan and J. Guo, *Nano Energy*, 2019, **63**, 103845.
30 S. Jiang, B. Hu, Z. Shi, W. Chen, Z. Zhang and L. Zhang, *Adv. Funct. Mater.*, 2020, **30**, 1908558.
31 Y. Zhou, S. Feng, P. Zhu, H. Guo, G. Yan and X. Li, *Chem. Eng. J.*, 2021, **415**, 128998.
32 S. Sun, D. He, P. Li, Y. Liu, Q. Wan, Q. Tan, Z. Liu, F. An, G. Gong and X. Qu, *J. Power Sources*, 2020, **454**, 227907.
33 X. Jiao, J. Yin, X. Xu, J. Wang, Y. Liu, S. Xiong, Q. Zhang and J. Song, *Adv. Funct. Mater.*, 2021, **31**, 2005699.
34 R. Kataoka, Y. Oda, R. Inoue, N. Kawasaki, N. Takeichi and T. Kiyobayashi, *J. Power Sources*, 2017, **346**, 128–133.
35 Z. Zhang, Z. L. Wang and X. Lu, *ACS Nano*, 2018, **12**, 3587–3599.
36 H. Wang, J. Fu, C. Wang, J. Wang, A. Yang, C. Li, Q. Sun, Y. Cui and H. Li, *Energy Environ. Sci.*, 2020, **13**, 848–858.

37 R. Zhu, Z. Wang, X. Hu, X. Liu and H. Wang, *Adv. Funct. Mater.*, 2021, **31**, 2101487.
38 H. Wiggers, Y. H. Sehlleier, F. Kunze, L. Xiao, S. M. Schnurre and C. Schulz, *Solid State Ionics*, 2020, **344**, 115117.
39 H. Liu, C. Wei, H. Peng, W. Ma, Y. Wang, L. Zhang, C. Liu, C. Ma and J. Shi, *Surf. Coat. Technol.*, 2021, **423**, 127606.
40 M. Zhang, L. Li, X. Jian, S. Zhang, Y. Shang, T. Xu, S. Dai, J. Xu, D. Kong, Y. Wang and X. Wang, *J. Alloys Compd.*, 2021, **878**, 160396.
41 K. Wang, S. Luo, Y. Wu, X. He, F. Zhao, J. Wang, K. Jiang and S. Fan, *Adv. Funct. Mater.*, 2013, **23**, 846–853.
42 Z. Fang, S. Duan, H. Liu, Z. Hong, H. Wu, F. Zhao, Q. Li, S. Fan, W. Duan and J. Wang, *Small*, 2021, 2105172.
43 C. Dai, G. Sun, L. Hu, Y. Xiao, Z. Zhang and L. Qu, *InfoMat*, 2020, **2**, 509–526.
44 A. C. Ezika, E. R. Sadiku, C. I. Idumah, S. S. Ray and Y. Hamam, *J. Energy Storage*, 2022, **45**, 103686.
45 D. Zhou, D. Shanmukaraj, A. Tkacheva, M. Armand and G. Wang, *Chem*, 2019, **5**, 2326–2352.
46 Q. Huang, D. Wang and Z. Zheng, *Adv. Energy Mater.*, 2016, **6**, 1600783.
47 K. Xia, Z. Zhu, H. Zhang, C. Du, J. Fu and Z. Xu, *Nano Energy*, 2019, **56**, 400–410.
48 Y. Yu, Z. Fang, Y. Luo, H. Wu, Q. Li, S. Fan and J. Wang, *Nanoscale*, 2020, **12**, 24259–24265.
49 A. Yadav, B. De, S. K. Singh, P. Sinha and K. K. Kar, *ACS Appl. Mater. Interfaces*, 2019, **11**, 7974–7980.
50 W. Liu, Z. Chen, G. Zhou, Y. Sun, H. R. Lee, C. Liu, H. Yao, Z. Bao and Y. Cui, *Adv. Mater.*, 2016, **28**, 3578–3583.
51 S. Xu, Y. Zhang, J. Cho, J. Lee, X. Huang, L. Jia, J. A. Fan, Y. Su, J. Su and H. Zhang, *Nat. Commun.*, 2013, **4**, 1543.
52 Y. Wu, S. S. Mechael, Y. Chen and T. B. Carmichael, *ACS Appl. Mater. Interfaces*, 2020, **12**, 51679–51687.
53 D. Wang, K. Wang, H. Wu, Y. Luo, L. Sun, Y. Zhao, J. Wang, L. Jia, K. Jiang, Q. Li, S. Fan and J. Wang, *Carbon*, 2018, **132**, 370–379.
54 K. Jiang, J. Wang, Q. Li, L. Liu, C. Liu and S. Fan, *Adv. Mater.*, 2011, **23**, 1154–1161.
55 L. Sun, W. Kong, H. Wu, Y. Wu, D. Wang, F. Zhao, K. Jiang, Q. Li, J. Wang and S. Fan, *Nanoscale*, 2016, **8**, 617–625.
56 Z. Fang, Y. Luo, H. Wu, L. Yan, F. Zhao, Q. Li, S. Fan and J. Wang, *Carbon*, 2020, **166**, 183–192.
57 Y. Luo, K. Wang, Q. Li, S. Fan and J. Wang, *Small*, 2020, **16**, 1–13.
58 Y. Yu, Z. Fang, Y. Luo, H. Wu, Q. Li, S. Fan and J. Wang, *Nanoscale*, 2020, **12**, 24259–24265.
59 K. Wang, Y. Wu, H. Wu, Y. Luo, D. Wang, K. Jiang, Q. Li, Y. Li, S. Fan and J. Wang, *J. Power Sources*, 2017, **351**, 160–168.
60 J. Wang, Z. Shi, Y. Luo, D. Wang, H. Wu, Q. Li, S. Fan, J. Li and J. Wang, *Nanoscale*, 2021, **13**, 6863–6870.
61 Y. Luo, N. Luo, W. Kong, H. Wu, K. Wang, S. Fan, W. Duan and J. Wang, *Small*, 2018, **14**, 1702853.
62 K. Jiang, Q. Li and S. Fan, *Nature*, 2002, **49**, 5246–5252.
63 K. Liu, Y. Sun, L. Chen, C. Feng, X. Feng, K. Jiang, Y. Zhao and S. Fan, *Nano Lett.*, 2008, **8**, 700–705.
64 R. Huang, Y. Xie, Q. Chang, J. Xiong, S. Guan, S. Yuan and G. Jiang, *Nano*, 2019, **14**, 1950078.
65 P. Bärmann, M. Diehl, L. Göbel, M. Ruttert, S. Nowak, M. Winter and T. Placke, *J. Power Sources*, 2020, **464**, 228224.
66 H. Wu, L. Zheng, J. Zhan, N. Du, W. Liu, J. Ma, L. Su and L. Wang, *J. Power Sources*, 2020, **449**, 227513.
67 J. Wang, H. Liu, H. Wu, Q. Li, Y. Zhang, S. Fan and J. Wang, *Carbon*, 2021, **177**, 181–188.
68 Y. Luo, K. Wang, S. Luo, F. Zhao, H. Wu, K. Jiang, Q. Li, S. Fan and J. Wang, *ACS Appl. Nano Mater.*, 2018, **1**, 2997–3005.
69 Y. Luo, H. Wu, L. Liu, Q. Li, K. Jiang, S. Fan, J. Li and J. Wang, *ACS Appl. Mater. Interfaces*, 2018, **10**, 36058–36066.
70 B. Vincent, *Adv. Colloid Interface Sci.*, 2012, **170**, 56–67.
71 A. P. Gavrilyuk, I. L. Isaev, V. S. Gerasimov and S. V Karpov, *Colloid Polym. Sci.*, 2020, **298**, 1–7.
72 A. Barhoum and A. S. H. Makhlouf, *Emerging Applications of Nanoparticles and Architecture Nanostructures*, Elsevier, Amsterdam, 2018.
73 R. Gao, J. Tang, K. Zhang, K. Ozawa and L. C. Qin, *Nano Energy*, 2020, **78**, 105341.
74 Y. Zhang, Y. Cheng, J. Song, Y. Zhang, Q. Shi, J. Wang, F. Tian, S. Yuan, Z. Su, C. Zhou, Y. Wang and S. Yang, *Carbon*, 2021, **181**, 300.
75 J. Niu, S. Zhang, Y. Niu, H. Song, X. Chen, J. Zhou and B. Cao, *J. Mater. Chem. A*, 2015, **3**(39), 19892–19900.
76 H. Mi, F. Li, C. He, X. Chai, Q. Zhang, C. Li, Y. Li and J. Liu, *Electrochim. Acta*, 2016, **190**, 1032–1040.
77 J. Yang, X. Wang, X. Wang, R. Jia and J. Huang, *J. Phys. Chem. Solids*, 2010, **71**, 448–452.
78 G. Mu, Z. Ding, D. Mu, B. Wu, J. Bi, L. Zhang, H. Yang, H. Wu and F. Wu, *Electrochim. Acta*, 2019, **300**, 341–348.
79 N. Ding, J. Xu and Y. X. Yao, *Solid State Ionics*, 2009, **180**, 222–225.
80 H. N. Si, J. C. Lim and J. K. Lee, *Electrochim. Acta*, 2012, **74**, 53–58.
81 H. Zhang, P. Zong, M. Chen, H. Jin, Y. Bai, S. Li, F. Ma, H. Xu and K. Lian, *ACS Nano*, 2019, **13**(3), 3054–3062.
82 H. Xu, Y. Wang, R. Chen, Y. Bai, T. Li, H. Jin, J. Wang and H. Xia, *Carbon*, 2020, **157**, 330–339.
83 N. Liu, X. Mamat, R. Jiang, W. Tong, Y. Huang, D. Jia, Y. Li, L. Wang, T. Wågberg and G. Hu, *Chem. Eng. J.*, 2018, **343**, 78–85.
84 Y. C. Zhang, Y. You, S. Xin, Y.-X. Yin, J. Zhang, P. Wang, X. Zheng, F.-F. Cao and Y. G. Guo, *Nano Energy*, 2016, **25**, 120–127.
85 Y. Sun, J. Lopez, H. W. Lee, N. Liu, G. Zheng, C. L. Wu, J. Sun, W. Liu, J. W. Chung, Z. Bao and Y. Cui, *Adv. Mater.*, 2016, **28**, 2455–2461.
86 F. Di, N. Wang, L. Li, X. Geng, H. Yang, W. Zhou, C. Sun and B. An, *J. Alloys Compd.*, 2021, **854**, 157253.
87 B. H. Park, J. H. Jeong, G. W. Lee, Y. H. Kim, K. C. Roh and K. B. Kim, *J. Power Sources*, 2018, **394**, 94–101.
88 X. Zhou, H. Xie, X. He, Z. Zhao, Q. Ma, M. Cai and H. Yin, *Energy Environ. Mater.*, 2020, **3**, 166–176.

89 Z. Zhang, F. Xi, S. Li, X. Wan, W. Ma, X. Chen, Z. Chen, R. Deng, J. Ji, H. J. Fan and C. Chong, *Mater. Today Energy*, 2021, **20**, 100671.
90 K. Feng, W. Ahn, G. Lui, H. W. Park, A. G. Kashkooli, G. Jiang, X. Wang, X. Xiao and Z. Chen, *Nano Energy*, 2016, **19**, 187–197.
91 Y. Xu, Y. Zhu, F. Han, C. Luo and C. Wang, *Adv. Energy Mater.*, 2015, **5**, 1400753.
92 P. Guan, J. Li, T. Lu, T. Guan, Z. Ma, Z. Peng, X. Zhu and L. Zhang, *ACS Appl. Mater. Interfaces*, 2018, **10**, 34283–34290.
93 W. Zhou, J. Chen, X. Xu, X. Han, M. Chen, L. Yang and S. I. Hirano, *ACS Appl. Mater. Interfaces*, 2021, **13**, 15216–15225.
94 N. Phattharasupakun, M. Cormier, C. Geng, M. Sawangphruk and J. Dahn, *J. Electrochem. Soc.*, 2021, **168**, 090564.

